Science Advances
AAAS

Supplementary Materials for

Shape-morphing into 3D curved surfaces with nacre-like composite architectures

Lishuai Jin *et al.*

Corresponding author: Shu Yang, shuyang@seas.upenn.edu

Sci. Adv. **8**, eabq3248 (2022)
DOI: 10.1126/sciadv.abq3248

The PDF file includes:

Other Supplementary Material for this manuscript includes the following:

1. Fabrication

All structures investigated in this study are fabricated from Tensylon HSBD30A plies (DuPont ^{TM}) with thickness $t = 155\ \mu m$. The Tensylon ply is comprised of cross-plied [0/90] solid state extruded ultra-high-molecular-weight polyethylene (UHMWPE) films with a polyolefin adhesive on one side of the film.

1.1. 2D specimens. We fabricate 2 types of 2D specimens (i.e., the dog bone specimens and the rectangular specimens, see their geometric parameters in Fig. S2C and Fig. 3A) with different cut distributions and characterize their in-plane strength via uniaxial tensile tests and bending properties using three-point bending tests. Each specimen is comprised of 8 plies with each ply containing one cut, except for the S2-2-2 specimens which have no cuts in the top and the bottom plies and the w/o cut specimens which have no cuts in all plies. To investigate the effect of cut distribution on the mechanical performance of the specimens, we mutate the number of overlapped cuts in the specimen by changing the position of the cut in each ply. See the geometric details of each specimen in Table S1.

Category	Descriptions
S6-2	The cuts are distributed at two positions which have 6 and 2 overlapped cuts, respectively.
S4-4	The cuts are evenly distributed at two positions with each one having 4 overlapped cuts.
S3-2-3	The cuts are arranged at three positions which have 3, 2 and 3 cuts overlapped, respectively.
S3-2-3-tabs	This specimen is similar to S3-2-3, with the exception of an additional tab ($l = 15$ mm) at the positions containing 3 overlapped cuts.
S2-2-2	This specimen has 6 cuts evenly distributed at 3 positions with 2 overlapped cuts at each position. The top and bottom plies have no cuts.
w/o cut	No cuts are introduced in this specimen. To avoid slip and delamination at the grips in tensile tests, the dog bone sample is limited to 2 plies thick. Bending tests use a rectangular sample comprised of 8 plies.

Table S1. Geometric descriptions defining the layup of 2D specimens. All parameters are defined in Fig. 3A of the main text, the distance between adjacent cuts is $L = 25$ mm.

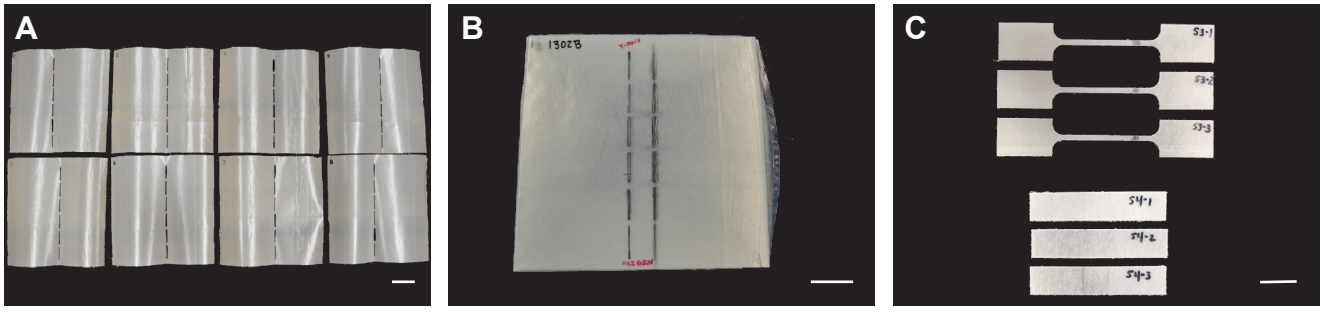

Fig. S1. Experimental snapshots of 2D specimens. (A) Slits are cut in the plies to introduce the discontinuities in the samples. (B) Slits are marked to verify the alignment of the plies. (C) Samples are cut out of the consolidated panels using a waterjet. Scale bars, 30 mm.

To fabricate the 2D samples we employ the following steps

- **Step A:** Cut the plies with embedded slit patterns using a Gerber cutting table. The slit locations correspond to discontinuities in the samples (Fig. S1A).

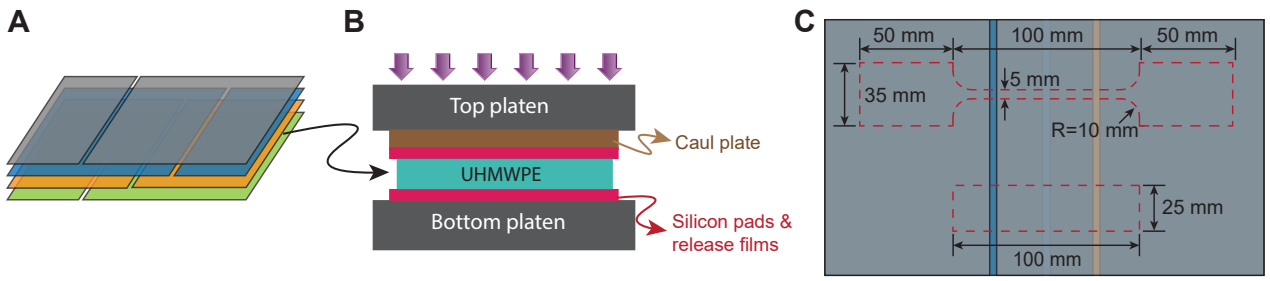

Fig. S2. Schematic of the fabrication for 2D specimens. (A) Plies are stacked together with prescribed slit alignment. (B) The stacked plies are consolidated in a press with a normal pressure of 20.7 MPa and a temperature of 110 ℃. (C) Samples with prescribed geometries are cut from the correct positions of the panel.

- **Step B:** Mark the slits using a permanent marker to verify sheet alignment and ensure samples are cut from the correct locations (Fig. S1B).
- **Step C:** Stack the plies (Fig. S2A) and consolidate them in a Wabash 800-ton (7.1 MN) press with a normal pressure of 20.7 MPa and a temperature of 110 °C (Fig. S2B). The complete high pressure, high temperature consolidation curves are given in Fig. S3A.
- **Step D:** Cut the samples out of the manufactured panels using a waterjet (Fig. S1C and Fig. S2C).

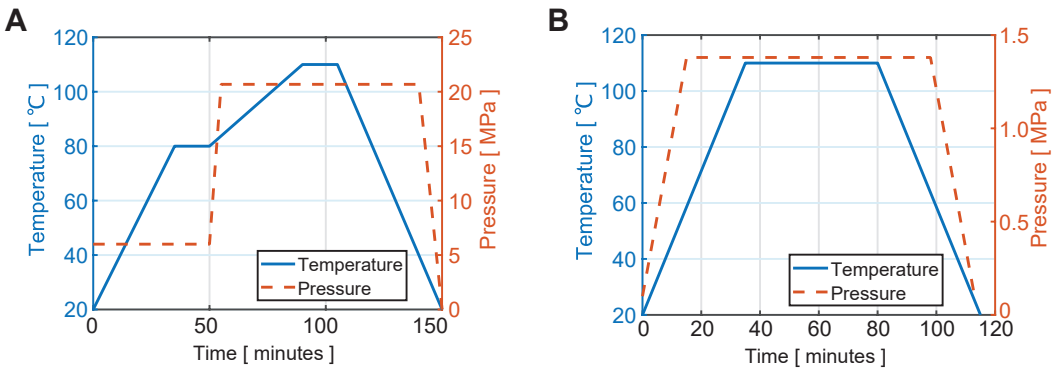

Fig. S3. Consolidation conditions for A) 2D specimens and B) 3D curved structures.

1.2. 3D curved structures. To fabricate the 3D curved structures with optimized mechanical performance, we first optimize the geometries of the 2D plies and then process the plies using the following steps

- **Step A:** Cut plies with the optimized geometries using a laser cutter (Universal Laser PLS 4.75, see the cut sample in Fig. S4A).
- **Step B:** Stack the plies into a 3D mold of the target geometry (inset of Fig. S4B). Mark the facets of each ply to verify the alignment and apply tapes to the top and bottom plies to facilitate the stacking (Fig. S4B).
- **Step C:** Wrap release films around the mold before putting them into a vacuum bag (Fig. S4C).

- **Step D:** Vacuum the bag and ensure the alignment of the plies is not changed during the vacuum process (Fig. S4D).
- **Step E:** Consolidate the plies in an autoclave under pressure of 1.38 MPa at 110 °C. (Fig. S4E). The conditions of the consolidation process are given in Fig. S3B.
- **Step F:** Remove the consolidated structure from the mold (Fig. S4F).

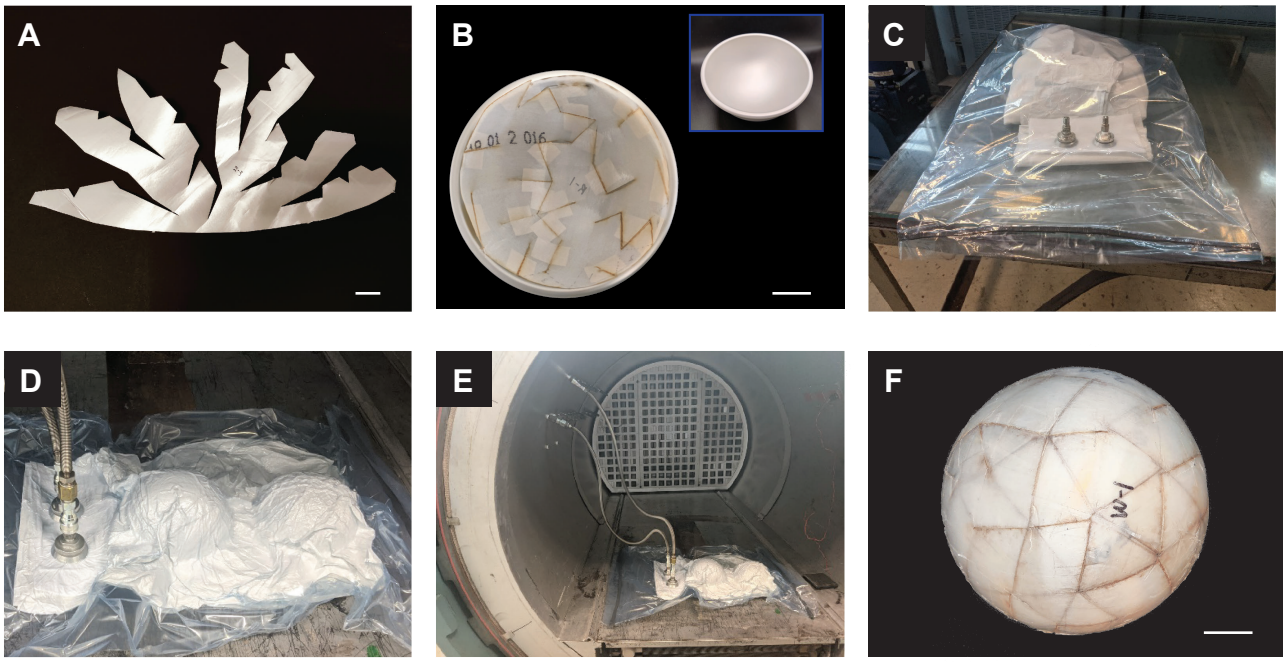

Fig. S4. Fabrication of the 3D curved structures. Snapshots of the 6 steps required to fabricate the structures. Scale bars, 30 mm.

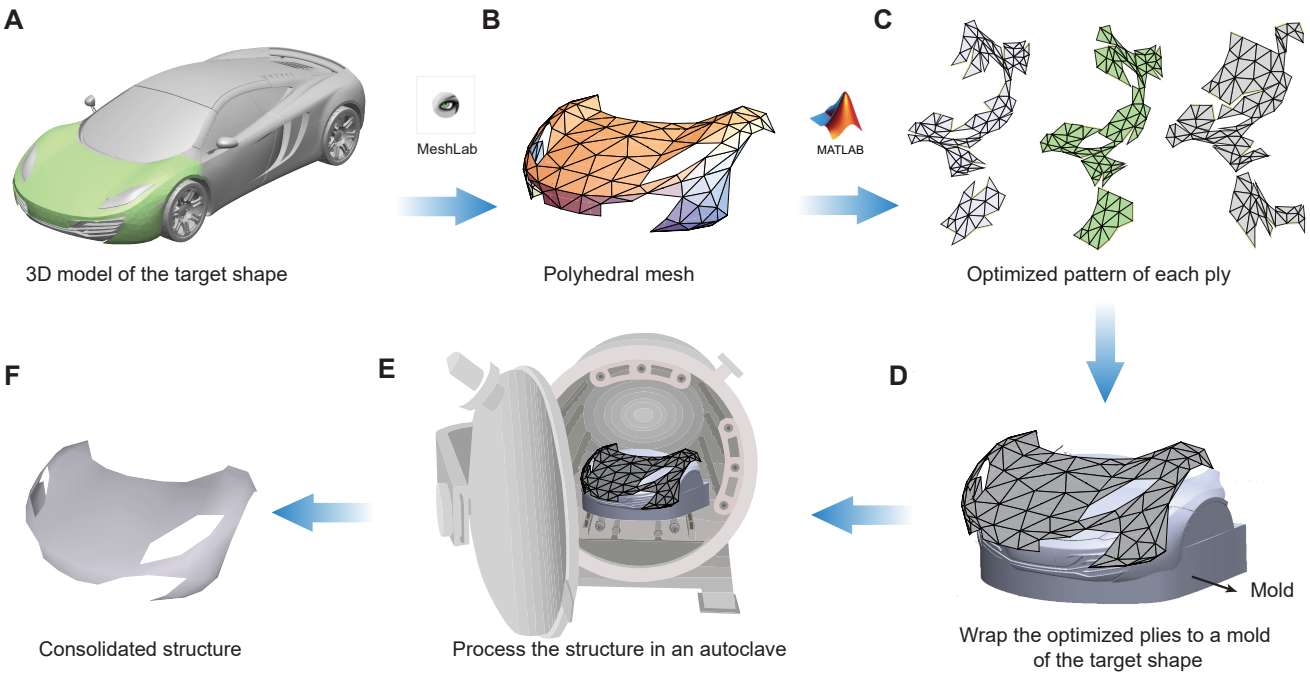

Fig. S5. Fabrication procedure for industrial applications. (A) Design 3D model of the target shape. (B) Discretize the target surface to a polyhedral mesh with appropriate mesh size. (C) Unfold the polyhedral mesh to a set of optimized 2D patterns using the algorithm proposed in this paper. (D) Cut composite plies to the optimized patterns and stack them in a mold of the target shape. (E) Transfer the plies and the mold into a vacuum bag and process the plies in an autoclave. (F) Remove the consolidated structure from the mold.

2. Experiments

All mechanical testing is performed using a universal testing machine (5564, Instron, Inc., USA)) equipped with a 2000N load cell for the tensile and compression tests and with a 100N load cell for the bending tests. The tests are performed under displacement control at a rate of 0.05 mm/s for the tensile tests and 0.2 mm/s for compression and bending tests.

2.1. Uniaxial tensile tests. The uniaxial tensile tests for dog bone specimens with different cut distributions are reported in Fig. S6. The results shown in Fig. S6B, C and D indicate that the cut distribution has a significant effect on the tensile strength of the specimens. Although the specimens S6-2, S4-4 and S3-2-3 have the same density of cuts, the S3-2-3 specimens show higher strength than the other two specimens proving the effectiveness of the optimization on cut distribution. Moreover, the higher strength of S3-2-3-tabs specimens than that of S3-2-3 specimens (shown in Fig. S6D and E) validates the enhancement of the mechanical strength provided by the tabs. Similar strength of the specimens shown in Fig. S6E and F also indicates that the tabs can eliminate the strength reduction induced by cuts, implying that the width of the tabs is large enough. The mean strength for the dog bone specimens with different layups is reported in Table S2. To better demonstrate the effect of cut distributions on the tensile strength, we also normalize the mean strength of each type of specimen by the strength of the one without cut.

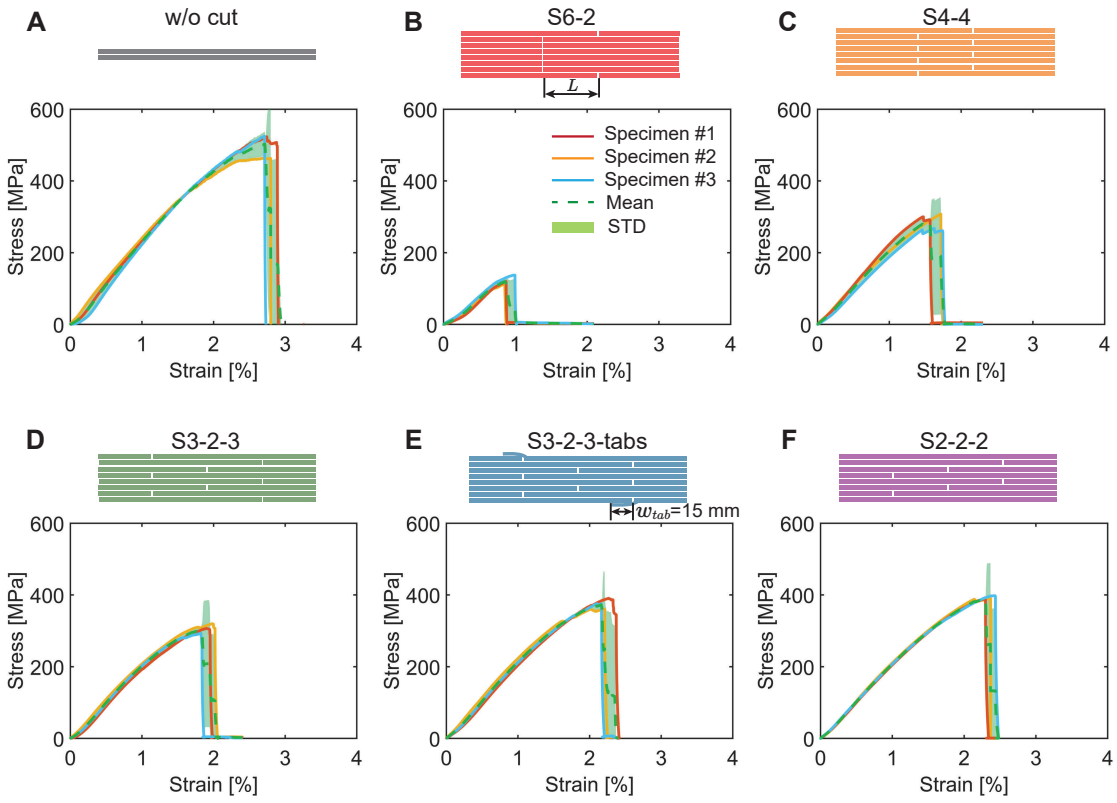

Fig. S6. Experimental stress-strain curves for dog bone specimens with different layups. Shaded areas indicate the standard deviation (STD) for the measurements.

2.2. Three-point bending tests. The resultant force of three-point bending tests for the laminated plies is sensitive to the relative position of the loading pin to the cuts in the specimens. In our

	w/o cut	S6-2	S4-4	S3-2-3	S3-2-3 tab	S2-2-2
Strength (mean) [MPa]	502.56	119.25	281.02	301.55	372.26	389.51
Normalized strength	1	0.237	0.559	0.600	0.741	0.775

Table S2. Tensile strength of dog bone specimens with different layups.

tests, we place the cuts beneath the loading pin and set the distance between the supporting pins as 50 mm (see schematic in Fig. S7). From the load-deflection curves reported in Fig. S7, we can see that the cut distribution has a significant effect on the bending property of the specimens and the peak forces decrease as the number of overlapped cuts increases. This trend is similar to that of the tensile testing, which validates the effectiveness of our approach on i) homogenizing the cut distribution and ii) mitigating the effect of cut by adding tabs. The absolute and normalized peak forces for the rectangular specimens with different layups are reported in Table S3.

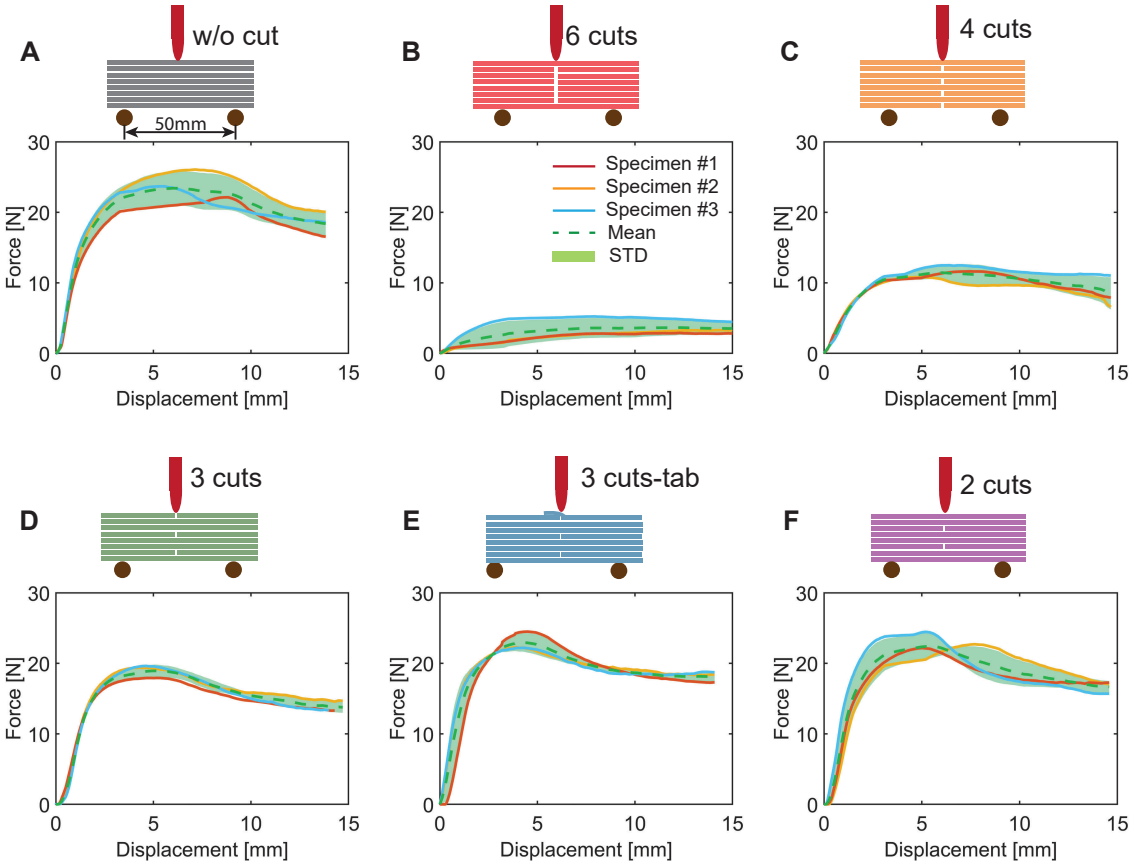

Fig. S7. Three-point bending curves for rectangular specimens with different layups. Shaded areas indicate the STD for the measurements.

2.3. Compression tests for 3D shells. To validate that the optimized 3D curved structure has better mechanical performance than the one with randomly designed cut distribution, we conduct compression tests for different structures under various loading conditions. Specifically, we conduct three sets of experiments, including: (i) Compression of hemispherical shells with different layups along the central line of the shells (Fig. 3E); (ii) Compression of hemispherical shells with different

	w/o cut	6 cuts	4 cuts	3 cuts	3 cuts-tab	2 cuts
Peak force (mean) [N]	23.39	3.63	11.45	18.92	22.95	22.40
Normalized peak force	1	0.155	0.490	0.809	0.981	0.958

Table S3. Peak forces of the rectangular specimens with different layups.

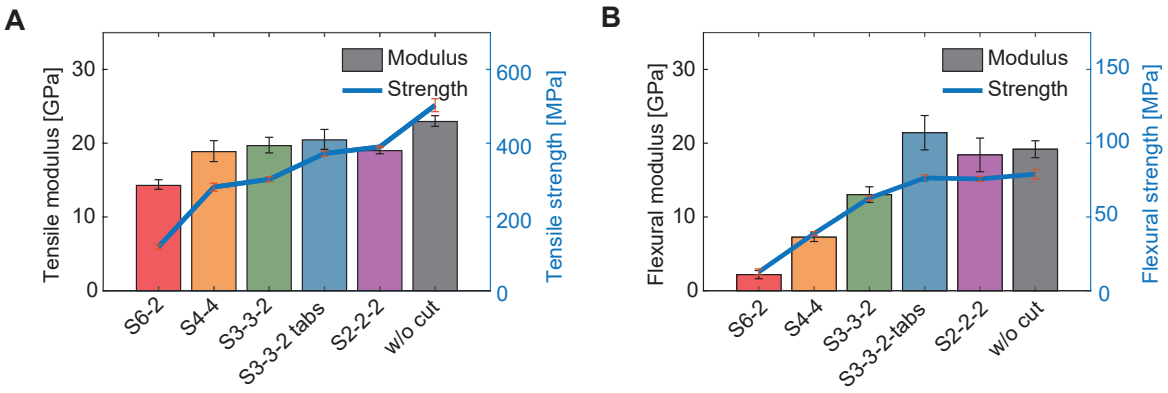

Fig. S8. Comparison of mechanical properties for 2D specimens with different cut distributions. (A) Tensile modulus and tensile strength of 2D dog bone specimens under uniaxial tensile tests. (B) Flexural modulus and flexural strength of 2D rectangular specimens under three-point bending tests.

layups along the direction that is perpendicular to the central line of the shells (Fig. 3F); (iii) Compression tests of face guards with different layups (Fig. 4F).

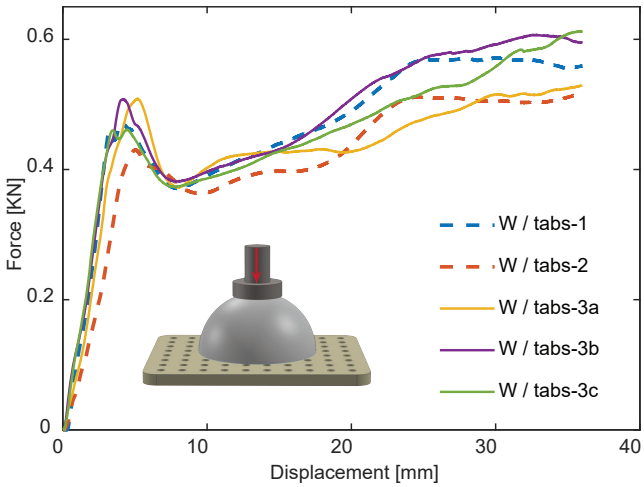

Fig. S9. Force-displacement curves of five spherical shells with different optimized design (including tabs) under compression tests. Specimens w/tabs-1, w/tabs-2 and w/tabs-3a have different geometries of the corresponding plies but all of them have no cuts overlapped in four layers. Specimens w/tabs-3a, w/tabs-3b and w/tabs-3c have the same geometries of the corresponding plies, but the stacking sequences among them are different. All specimens exhibit good consistency in their force-displacement curves under compression.

3. Modeling

In this section, we provide details of our model on investigating the impact of cut distributions on mechanical properties of the composite plies and unfolding 3D curved surfaces to 2D nets, as well as optimizing the geometries of 2D nets to realize prescribed 3D curved structures with optimal mechanical performance.

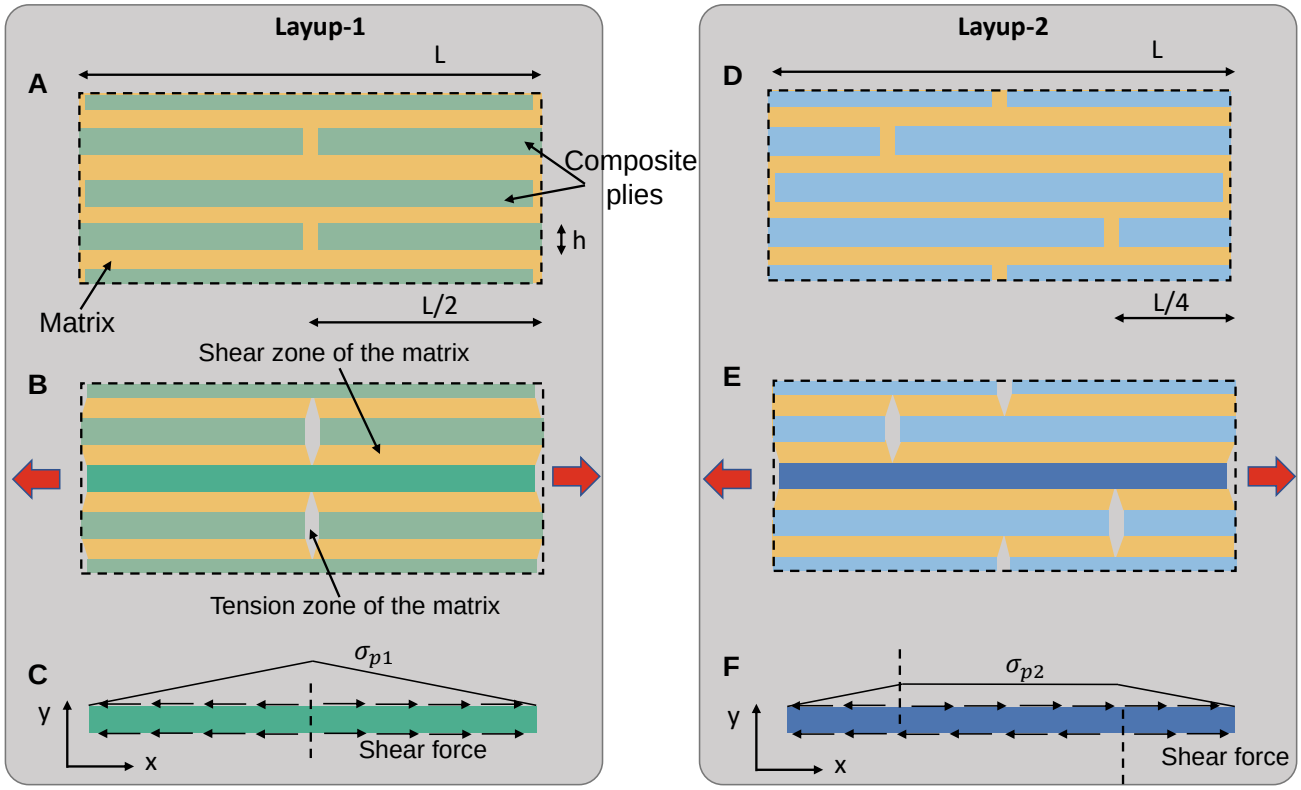

Fig. S10. Simplified models for stacked plies with different layups. (A-C) The cuts of the plies repeat in every two layers at the same position. (D-F) The cuts of the plies repeat in every four layers at the same position.

3.1. Effect of cut distributions on mechanical properties of the composite plies. Our algorithm is proposed to design 3D doubly curved structures with high mechanical performance, which is difficult to investigate analytically due to the various geometries of the target surfaces. Nevertheless, the principle and effectiveness of homogenizing cut distribution can be demonstrated in 2D structures under simple loading conditions. To investigate the impact of cut distributions on mechanical properties of the composite plies, we extend a one-dimensional biocomposites model proposed by Gao et al. (34, 46) and compare two composite structures comprising the same plies but different layups (see schematic in Fig. S10A and D), and investigate the modulus and strength of these two stacked plies under tensile loads.

The first layup has cuts repeating in every two layers at the same positions (see the representative elementary volume (REV) of layup-1 in Fig. S10A). We denote the length and height of the composite plies as L and h, respectively. Under an applied tensile stress, the composites plies carry most of the tensile load while the matrix transfers the load between plies via shear (Fig. S10B). Refer to the pioneering work by Gao et al. (34, 46), we assume that the stress distribution along the length of the plies is linear (Fig. S10C). Hence, the maximum stress σ_{p1} and average stress $\bar{\sigma}_{p1}$ in the plies yield

$$\sigma_{p1} = \rho\tau_{m1}, \quad \bar{\sigma}_{p1} = \rho\tau_{m1}/2, \tag{S1}$$

where $\rho = L/h$ represents the aspect ratio of the composite ply with $\rho >> 1$, and τ_{m1} is the shear stress of the matrix. According to Fig.S10B, the matrix does not carry tensile load, hence the effective tensile stress σ_1 of the REV can be expressed as

$$\sigma_1 = \phi\bar{\sigma}_{p1}, \tag{S2}$$

where ϕ represents the volume fraction of the plies to the REV. The effective strain of the REV is induced by the tensile deformation of the composite plies and the shear deformation of the matrix, which can be expressed as

$$\varepsilon_1 = \frac{\Delta_{p1} + 2\gamma_{m1}h(1-\phi)/\phi}{L}, \tag{S3}$$

where Δ_{p1} and γ_{m1} are the extension of the composite plies and the shear strain of the matrix, which can be written as

$$\Delta_{p1} = \frac{\sigma_{p1}L}{2E_p}, \quad \gamma_{m1} = \frac{\tau_{m1}}{\mu_m}, \tag{S4}$$

where E_p is the Young's modulus of the plies and μ_m is the shear modulus of the matrix. According to Eqs. S1-S4, one can derive the effective tensile modulus E_1 of the REV with layup-1 as

$$\frac{1}{E_1} = \frac{1}{\phi E_p} + \frac{4(1-\phi)}{\mu_m\phi^2\rho^2}. \tag{S5}$$

The second layup has cuts repeating in every four layers at the same positions (see the REV of layup-2 in Fig. S10D) and the stress distribution in each composite ply is different from that of the layup-1 due to the different cut distribution (Fig. S10F). Hence, the maximum stress σ_{p2} and average stress $\bar{\sigma}_{p2}$ in the plies yield

$$\sigma_{p2} = \rho\tau_{m2}, \quad \bar{\sigma}_{p2} = 3\rho\tau_{m2}/4, \tag{S6}$$

where τ_{m2} is the shear stress of the matrix in layup-2. The effective stress and effective strain of layup-2 can be expressed as

$$\sigma_2 = \phi\bar{\sigma}_{p2}, \tag{S7}$$

$$\varepsilon_2 = \frac{\Delta_{p2} + 2\gamma_{m2}h(1-\phi)/\phi}{L}, \tag{S8}$$

and the extension of the composite plies and the shear strain of the matrix in layup-2 yields

$$\Delta_{p2} = \frac{3\sigma_{p2}L}{4E_p}, \quad \gamma_{m2} = \frac{\tau_{m2}}{\mu_m}. \tag{S9}$$

Combining Eqs. S6 - S9 yields the effective tensile modulus E_2 of layup-2 as

$$\frac{1}{E_2} = \frac{1}{\phi E_p} + \frac{8(1-\phi)}{3\mu_m \phi^2 \rho^2}. \quad [S10]$$

And the ratio between E_1 and E_2 reads

$$\frac{E_1}{E_2} = 1 - \frac{4(1-\phi)\phi E_p}{3(\mu_m \phi^2 \rho^2 + 4(1-\phi)\phi E_p)}. \quad [S11]$$

Since all parameters in Eq. S10 are positive and $\phi < 1$, the ratio between E_1 and E_2 is less than 1, representing layup-2 with less cuts overlapped at the same position have higher modulus than layup-1. To validate the accuracy of our simplified model, we conduct finite element simulations to characterize the tensile modulus of these two REVs and report the evolution of the normalized modulus as a function of the aspect ratio ρ in Fig. S11A. In our simulations, we use $\phi = 0.889$, $E_p = 23$ GPa and $\mu_m = 303$ MPa. From the plots we find excellent agreement between simulations and theoretical predictions, the effective modulus increases as the aspect ratio ρ becomes larger and the modulus of layup-2 is always larger than layup-1 (with the exception of the simulation results for $\rho = 10$).

Furthermore, to evaluate the strength of the REVs comprising different layups, we compare the evolution of tensile stress along the length of the composite plies in Fig. S11B. Both FE results and theoretical predictions show that the layup-2 has smaller peak stress when a 2% strain is applied to the structures, indicating that higher strength can be achieved when cuts are more homogeneously distributed in the structures.

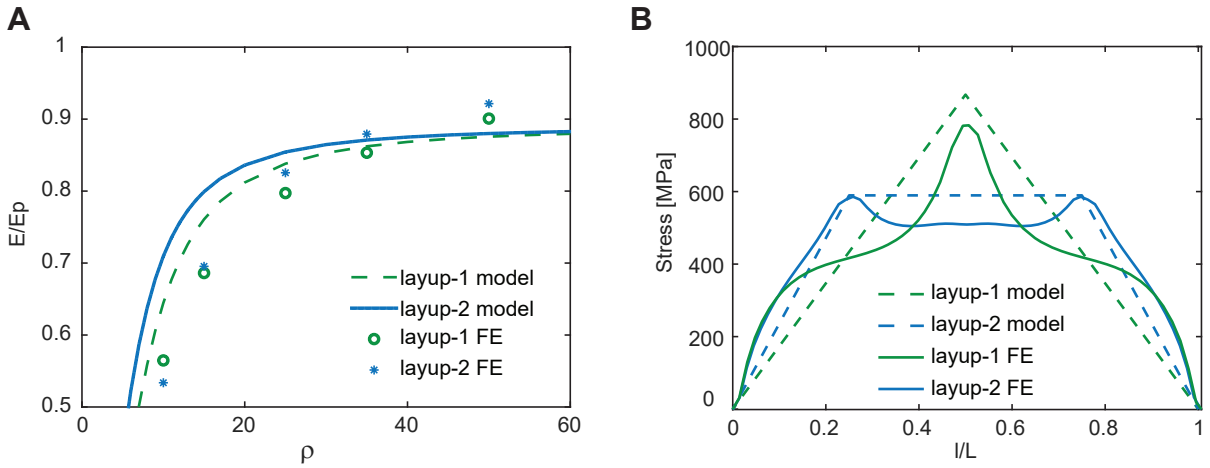

Fig. S11. Validation of the model. (A) Comparison of the Young's modulus of the REVs prediced by our model and by FE simulations. (B) Stress distribution in each composite ply of the REVs when a 2% tensile strain is applied to the REVs.

3.2. Unfolding 3D curved surfaces to 2D nets. To unfold curved surfaces into valid 2D nets without self-overlapping, we employ the following steps (see schematic in Fig. 2A of the main text):

- **Discretize the surface to a mesh.** Discretize a given smooth surface to a triangular mesh using the open source software MeshLab. The number of the triangular facets of the mesh

can be controlled by setting the target number of faces during the mesh generation. In our study, we set the number of the facets $N \in [50, 100]$ to obtain good conformability, reasonable computational cost and high mechanical strength.

- **Generate the cutting graph.** Represent the polyhedral mesh using a cutting graph (dual graph). The cutting graph contains all edges of the mesh and elucidates the connection among the facets of the polyhedral mesh (i.e., the vertices and lines of the cutting graph correspond to the facets and edges of the polyhedral mesh, respectively).

- **Unfold the mesh to nets.** With the cutting graph, one can unfold the mesh to a 2D net by calculating the minimum spanning tree (MST), which is a subset of the edges of the cutting graph that connects all the vertices together without any cycles, and with the minimum total edge weight. By assigning a set of weights to the edges of the cutting graph, we can generate a specific cutting path via the MST. If the edges of the mesh belong to the MST, the edges are used for unfolding. Otherwise, the edges will be cut. In this study, the MST is computed from the cutting graph using the Prim's algorithm (38).

  Moreover, the unfolding net is typically not a valid net that contains multiple overlaps. To obtain valid nets without a overlap, we detect the overlap of each unfolded net by checking if any facets of the nets intersect with each other (39). To facilitate the generation of non-overlapping nets, we employ different algorithms (including breadth-first unfolding, steepest-edge unfolding, flat-tree unfolding and random-shortest-path unfolding) to assign the weights for the cutting graph. Note that other algorithms can also be readily embedded into our model.

- **Add tabs to the nets.** To mitigate the cut induced shear lag effect on the mechanical performance of the reconstructed structures, we also add tabs to the cut edges of the 2D nets. Each tab has a trapezoidal geometry which is trimmed from the corresponding triangular facet of the cut edge (see tabs i and j and their corresponding facets i' and j' in Fig. S12). With this design, the tabs will not overlap with each other after the plies are wrapped to 3D structures. Moreover, the tabs should have a minimum width w_{tag} to provide enough shear forces to mitigate the mechanical weakness induced by the cuts, but the tags should not be too large since that would cause additional overlaps and, in turn, limit the design space to find the optimized nets. Further, only one tab is added for each pair of the cut edges (see illustration of paired cut edges $a - b$ and $c - d$ in Fig. S12).

3.3. Optimization of the cuts for the plies. After demonstrating the procedure to realize valid 2D nets from a given 3D surface, we then optimize the cut distribution of each ply to minimize the number of overlapped cuts in the stacked plies. We illustrate the algorithm using a flow chart in Fig. S13 and describe the details of the algorithm in following steps:

- **Step 1:** Approximate the 3D surface using a triangular mesh and calculate the cutting graph for the mesh.

- **Step 2:** Assign weights to the cutting graph using different algorithms (breadth-first unfolding, steepest-edge unfolding, flat-tree unfolding and random-shortest-path unfolding) to facilitate the generation of 2D nets without overlap, and unfold the 3D mesh using MST of the cutting graph. Note that we set the weights calculated from these algorithms larger than 1 to differentiate the weight of the edge containing cut in Step 4.

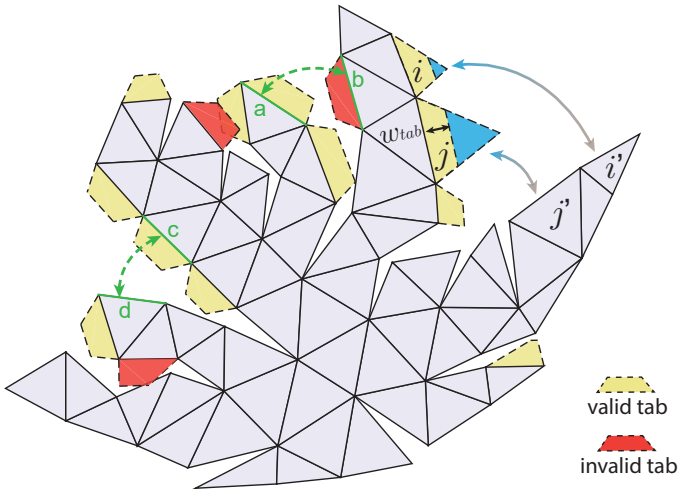

Fig. S12. Design of the tabs. The tabs of the plies are trimmed from the corresponding triangular facets of the cut edges with a minimum width w_{tag} (see tabs i and j and their corresponding facets i' and j'). Tabs are invalid and will not be kept if i) they overlap with the triangular facets or other tabs and ii) two tabs are assigned for one pair of cut edges (see tabs with red color).

- **Step 3:** Check whether the 3D mesh contains hyperbolic nodes. If the mesh contains hyperbolic nodes, introduce minimum number of additional cuts to the unfolded 2D net to avoid self-overlap induced by the hyperbolic nodes and check if the new net, which typically comprises multiple patches, is a overlap-free net. Otherwise, check the overlap of the net directly. If the net is not overlap-free, repeat Step 2 and Step 3 until a overlap-free net is found. Then, add tabs to the valid net.

- **Step 4:** Optimization of other plies. Check the number of overlapped cuts of the optimized ply (plies), if more than one cut overlaps at the same edge. The optimization procedure will be restarted from Step 2. Otherwise, assign a small weight (0.01) to the edges of the cutting graph that contain one cut among the plies, and update the weights of other edges using the algorithms mentioned in Step 2. Note that we assume that the cut can be ignored if a tab is assigned. When calculating the MST for the next ply, the edges containing cut (with small weight of 0.01) will largely not be cut again. Then, the overlap of the new ply will be checked and tabs will be added to the valid ply accordingly. This procedure will be repeated until the target number of plies n_{max} is achieved.

- **Step 5:** Output the optimized plies.

Note that, to realize a structure comprising more than n_{max} plies, one can simply stack the optimized plies until the target thickness is reached. The optimization algorithms are implemented in Matlab.

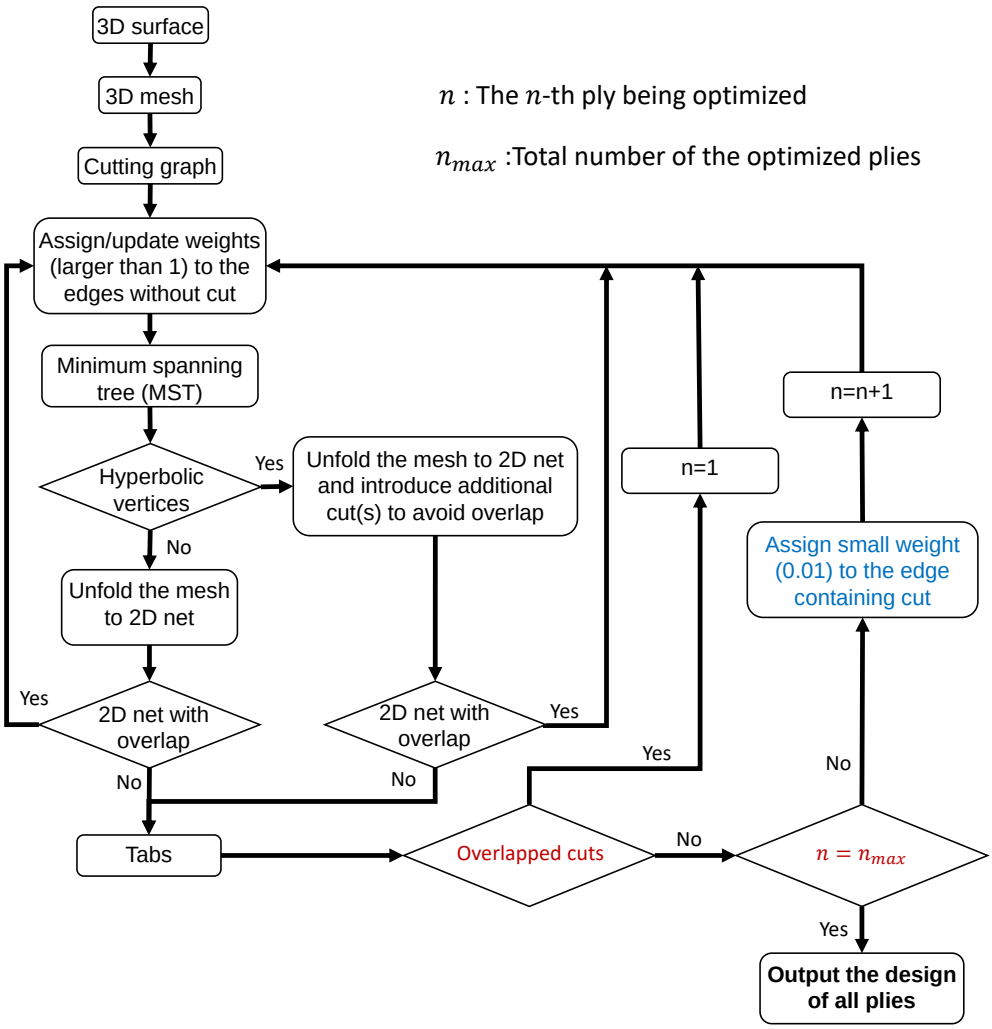

Fig. S13. Flow chart of the optimization procedure.

4. Additional results

In this section, we demonstrate the capability of our model for the optimization of diverse structures, including a semi-ellipsoidal surface (Fig. S14), a helmet (Fig. S15) and a racing seat (Fig. S16).

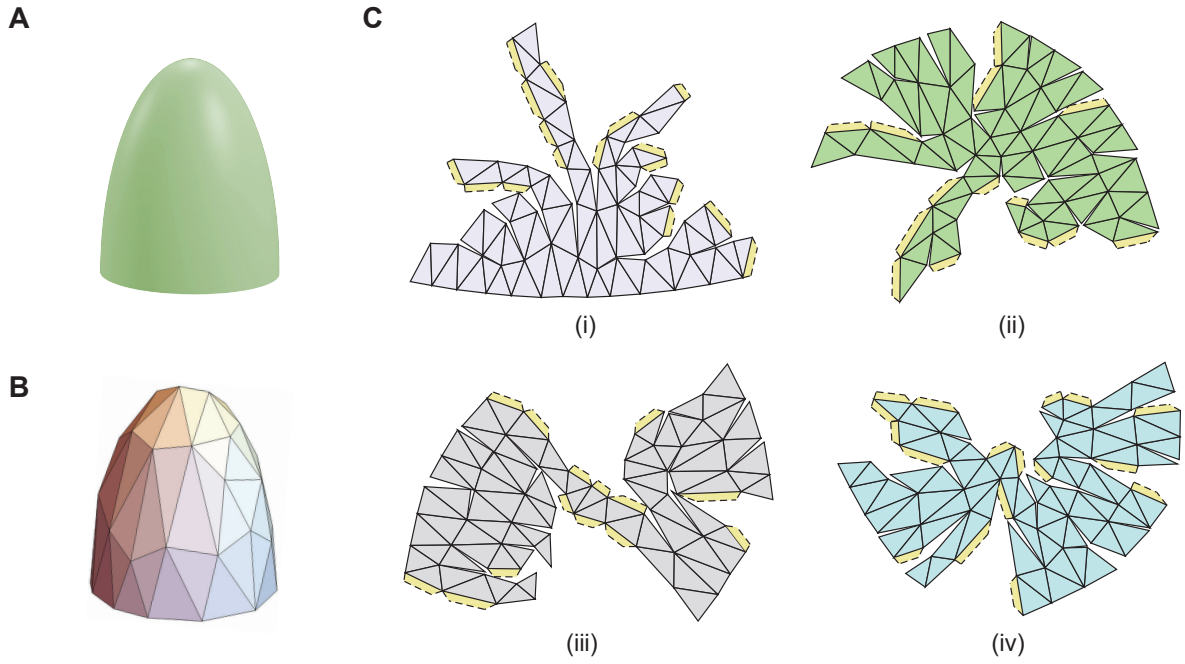

Fig. S14. Optimized design for the semi-ellipsoidal surface. (A) The target surface. (B) Discretize the target surface using triangular facets. (C) A set of the optimized plies, which have no cut overlapped at the same position when folded and stacked into the target surface.

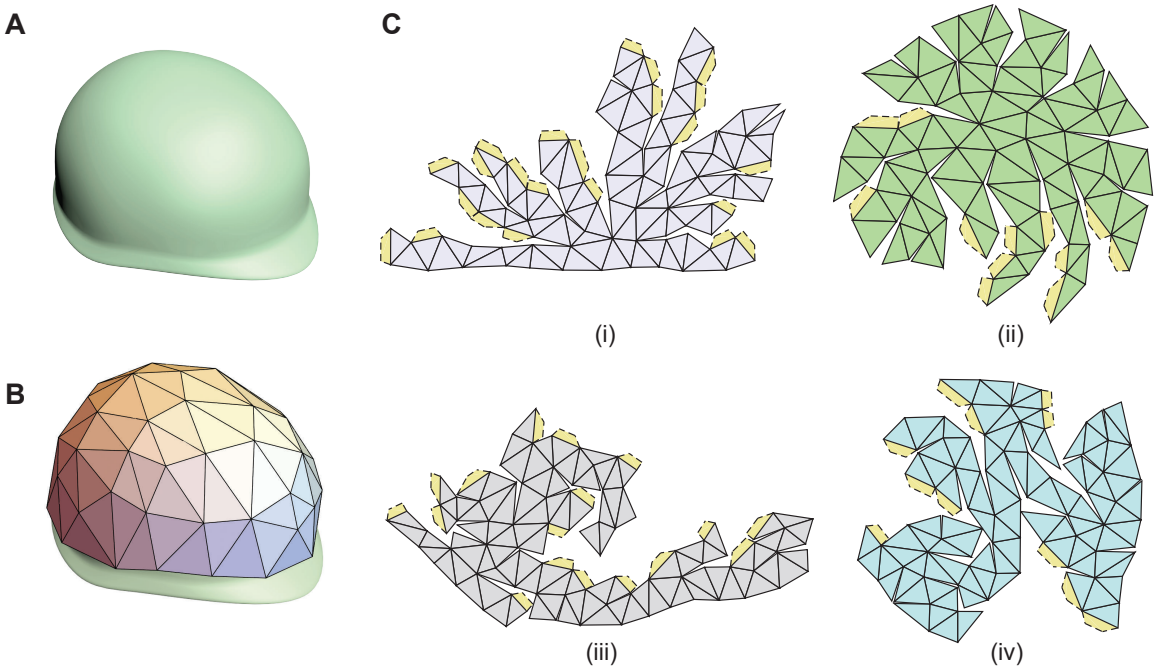

Fig. S15. Optimized design for the helmet. (A) The target surface. (B) Discretize the target surface using triangular facets. (C) A set of the optimized plies, which have no cut overlapped at the same position when folded and stacked into the target surface.

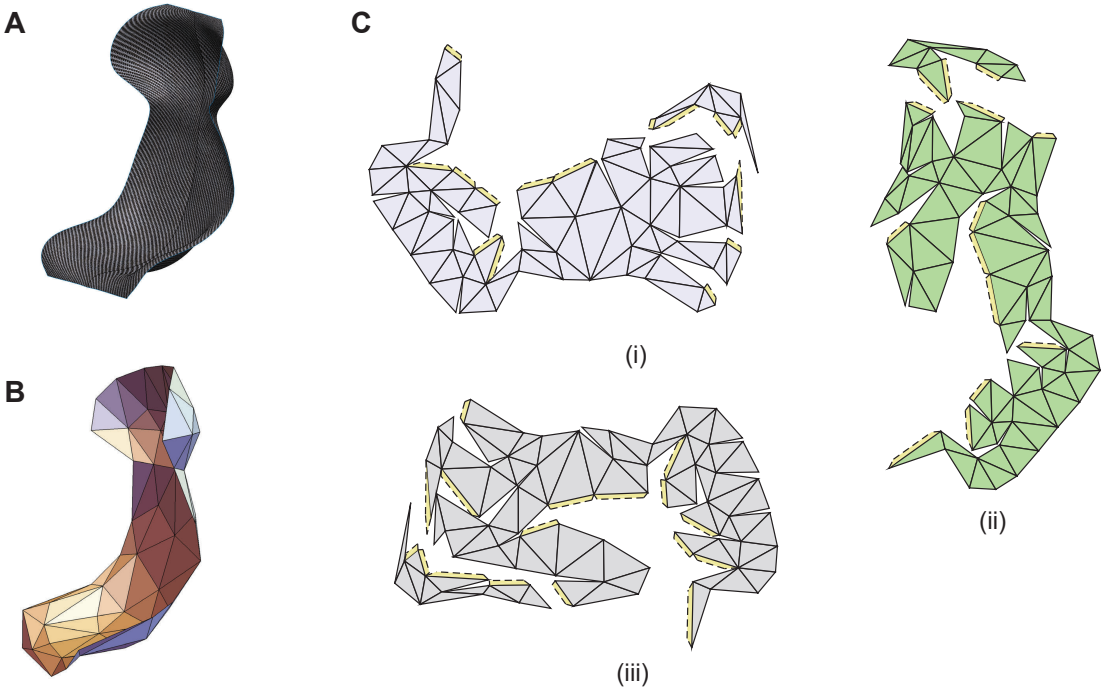

Fig. S16. Optimized design for the racing car seat. (A) The target surface. (B) Discretize the target surface using triangular facets. (C) A set of the optimized plies, which have no cut overlapped at the same position when folded and stacked into the target surface.

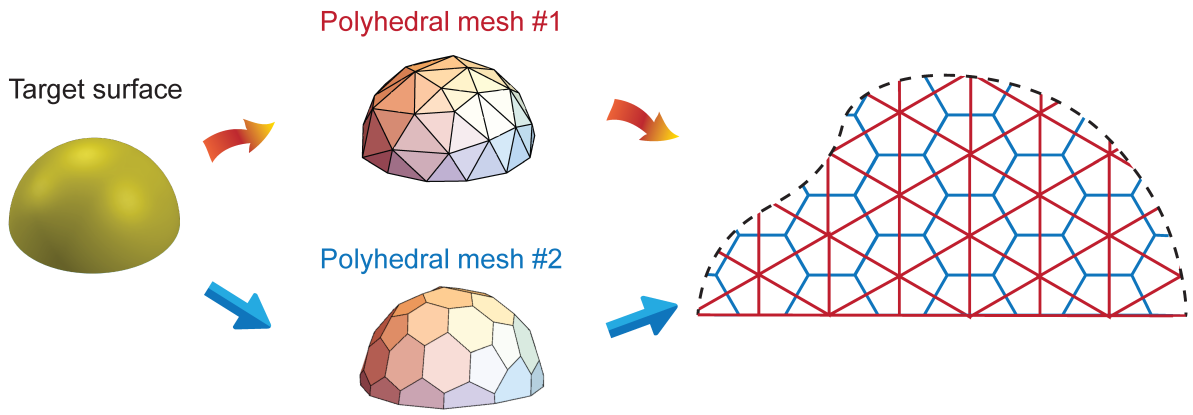

Fig. S17. Discretize the smooth surface using different meshes. The edges of these two meshes are mutually orthogonal with each other. Plies generated from these two meshes are free of overlapping on cuts.

Movie S1. Comparison of the cut distribution for multi-plied hemispheres with different layups.

For the hemispheres comprising 4 plies, the random design has 4 cuts overlapped at some position, while the optimized design has at most 2 cuts overlapped at the same positions, and the optimized design with tabs has no cut overlapped in 4 plies, enhancing the mechanical performance of the resulting structure by leveraging the interlaminar shear between the plies.

Movie S2. Compression tests of hemispherical shells with different layups.

Each sample consists of 8 plies of Tensylon HSBD30A laminates. The optimized design with tabs exhibits the best mechanical performance in comparison to the optimized design without tabs and the random design.

Movie S3. Optimized layup for a semi-ellipsoid.

Demonstration of the cut distribution for a semi-ellipsoidal shell with 4 plies of optimized layup.

Movie S4. Optimized layup for a helmet.

Demonstration of the cut distribution for a helmet with 4 plies of optimized layup.

Movie S5. Optimized layup for a face guard.

Demonstration of the cut distribution for a face guard with 3 plies of optimized layup.

Movie S6. Optimized layup for a racing car seat.

Demonstration of the cut distribution for a racing car seat with 3 plies of optimized layup.